AIAA AVIATION Forum
17-21 June 2019, Dallas, Texas
AIAA Aviation 2019 Forum

10.2514/6.2019-3168

Check for updates

High Control Authority 3D Aircraft Control Surfaces Using Co-Flow Jet

Kewei Xu *, Gecheng Zha †
Dept. of Mechanical and Aerospace Engineering
University of Miami, Coral Gables, Florida 33124
E-mail: gzha@miami.edu

Downloaded by Gecheng Zha on June 22, 2019 | http://arc.aiaa.org | DOI: 10.2514/6.2019-3168

Abstract

This paper numerically studies the performance of 3D Co-flow Jet (CFJ) control surfaces to achieve ultra-high control authority with zero-net-mass-flux flow control at low energy expenditure. The effects of CFJ moment coefficient (C_μ), sideslip angle (β) and deflection angle (δ) are investigated. The 3D swept vertical tail tested by Selee et al is used as the baseline for comparison. Numerical study is conducted with unsteady simulation due to the highly unsteady flow of the tip vortex induced by the low aspect ratio swept control surface and the vortex generated by the gap between the control surface root and the wall. The high fidelity in-house CFD code FASIP with the Improved Delayed Detached Eddy Simulation (IDDES) turbulence modeling is utilized. The predicted lift and drag coefficients achieve a good agreement with experiment for the baseline control surface with the maximum discrepancy less than 3.8%. The numerical simulation indicates that applying co-flow jet on control surface is very effective and energy efficient. A small C_μ of 0.025 generates a 28% C_L increment at 0 sideslip angle with a higher corrected aerodynamic efficiency ($(C_L/C_D)_c$) than the baseline case. With the C_μ of 0.26, the C_L is increased by 99.25% at 0 sideslip angle and the C_D drops 52% due to removal of the flow separation and suppression of the tip and root vortices by the co-flow jet. A phenomenon not observed in a regular CFJ wing without flap is that the second pressure suction peak at the flap shoulder is higher than the leading edge suction peak. It is attributed to the attached flow experiencing a rapid turning due to the flap deflection, which creates a local acceleration that significantly reduces the pressure. The CFJ control surface also has much higher stall margin than the baseline control surface. With C_μ=0.26, the CFJ control surface stalls at the sideslip angle of 27.5°, which is 2.2 times higher than that of the baseline control surface of 12.5° and a very high C_L of 2.84 is also achieved. Furthermore, with C_μ=0.26 and zero sideslip angle, a very high C_L of 1.88 and 2.12 is achieved at δ=40° and 50°, which is 2.3 and 2.5 times of the baseline cases respectively.

Nomenclature

AoA	Angle of attack
AFC	Active Flow Control
C	Chord length
CFJ	Co-flow jet
C_L	Lift coefficient
C_D	Drag coefficient
$(C_D)_c$	Drag coefficient corrected for CFJ airfoil
C_p	Constant pressure specific heat

* Ph.D. Candidate
† Professor, ASME Fellow, AIAA associate Fellow

Copyright © 2019 by all the authors of this paper . Published by the American Institute of Aeronautics and Astronautics, Inc., with permission.

C_μ	Jet momentum coef. $\dot{m}_j\, U_j/(q_\infty\, S)$
C_L/C_D	Aerodynamic efficiency
$(C_L/C_D)_c$	Aerodynamic efficiency corrected for CFJ airfoil
D	Total drag on the airfoil
$FASIP$	Flow-Acoustics-Structure Interaction Package
H_t	Total enthalpy
L	Total lift on the airfoil
LE	Leading Edge
$\dot{m}$	Mass flow
M	Mach number
MAC	mean aerodynamic chord
P	CFJ Pumping power
P_c	Power coefficient $L/(q_\infty\, S\, V_\infty)$
P_t	Total pressure
$RANS$	Reynolds-Averaged Navier-Stokes
R_e	Reynolds number
S	Planform area of the wing
TE	Trailing Edge
T_t	Total temperature
V_∞	Freestream velocity
$ZNMF$	Zero-Net Mass Flux
c	Subscript, stands for corrected
j	Subscript, stands for jet
α	Angle of attack
β	Sideslip angle
γ	Air specific heats ratio
ρ_∞	Freestream density
δ	Deflection angle
θ_1	Angle between the injection slot surface and a line normal to the airfoil chord
θ_2	Angle between the suction slot surface and a line normal to the airfoil chord

Downloaded by Gecheng Zha on June 22, 2019 | http://arc.aiaa.org | DOI: 10.2514/6.2019-3168

1 Introduction

Aircraft control surfaces such as vertical tails, horizontal tails, and canards are responsible for maintaining the aircraft stability. Control surfaces need to have high control authority by generating sufficient lift with rapid response time to keep the aircraft trimmed. To achieve such performance, the control surfaces usually have large sizes, which bring severe penalty of weight, drag, and energy consumption.

Active Flow Control (AFC) as a mean to enhance lift has great potential to reduce the size and weight of control surfaces [1, 2, 3, 4, 5, 6, 7]. AFC is used to control the separated flow of vertical tails to enhance aerodynamic performance and mitigate flutter [8, 9, 10, 11, 12, 13, 14, 15, 16, 17]. The research of Boeing and NASA in [8, 9, 10, 11, 12, 13, 14, 15] on vertical tails using sweeping jets and synthetic jets AFC represents the state of the art. Rathay et.al [8] conducted wind tunnel experiments on a swept and tapered tail with a 29.6% chord rudder. Using flow control, the side force was increased by up to 18% at moderate rudder deflections with actuators operating at dimensionless frequency of O (10) [8] and a momentum coefficient C_μ=0.721%. Compared

with synthetic jets, sweeping jets have higher C_μ output and corresponding jet velocity. Thus sweeping jets were selected over the synthetic jets by Boeing/NASA team for the subsequent full-scale AFC wind tunnel tests [9, 10].

The vertical tails with sweeping jet AFC were successfully tested on subscale [11, 12], full-scale models [9, 10] and finally in flight [9]. The subscale test was performed at a 14% scale model of Caltech and more than 50% side force enhancement was achieved by sweeping jet actuation with the momentum coefficient C_μ of 1.7%. The full-scale vertical tail model equipped with sweeping jet AFC was tested at a nominal speed of 100 knots ($M_\infty \sim 0.15$, Re $\sim$ 15 million), a maximum speed of 130 knots ($M_\infty \sim 0.2$, Re $\sim$ 20 million), and across the vertical tail flight envelop for rudder deflections (0° to 30°) and sideslip angles (0° to −7.5°). A 31-actuator AFC configuration produces significant flow attachment on the rudder, which results in 20% increase in side force for the maximum rudder deflection of 30° at 0 and −7.5° sideslip angles. Subsequently, the sweeping jet-enhanced vertical tail was flown on the Boeing 757 ecoDemonstrator in the spring of 2015. A side force increase of 13% to 16% was estimated at 30° rudder deflection for critical sideslip range between $\beta = 0°$ and −7.5° with the activation of AFC. Kara [16, 17] analyzed the complex flow inside the sweeping jet for design optimization of actuator geometry with minimum pressure loss. However, these studies [8, 9, 10, 11, 12, 13, 14, 15, 16, 17] do not report sufficient results on energy expenditure of the sweeping jets, which tend to suffer large energy loss due to jet sweeping, turning, and flow separation. Furthermore, the system energy penalty due to introducing the air flow mass from engine bleed is not given. The other challenging issue using engine bleed for flow control is that when the engines are idle at landing, the engines may not be able to provide sufficient mass flow.

Recently, Zhang et al [18] conducted 2D numerical simulation to study a new aircraft control surfaces using Co-flow Jet (CFJ) airfoil [2, 5, 19, 20, 21, 22, 23, 24, 25, 26, 27, 28], which is a zero-net mass flux (ZNMF) flow control that does not need to use engine bleed. The CFJ control surface is proven to be very effective at low energy expenditure. It could substantially reduce the control surface size and weight and simplify the control surface system. Xu et al [29] studied the energy expenditure of CFJ control surfaces. The parametric study of injection slot size and slot location is conducted to acquire the optimum aerodynamic efficiency of CFJ actuators. Besides, they also proposed two methods to minimize the CFJ control surface drag when it is not in use at cruise condition. One method is to use a very light jet at cruise and the other method is to cover the slots using a small moving surface segment. Previous CFJ control surface studies [18, 29] are mainly focused on 2D cases, which do not reflect the complexity of 3D control surface with sweep, low aspect ratio and being tapered.

The objective of this paper is to apply CFJ to a realistic 3D vertical control surface to demonstrate its superior performance. The 3D swept vertical tail tested by Selee et al [12] is used as the baseline for comparison. The effects of co-flow jet moment coefficient (C_μ), deflection angle (δ) and sideslip angle (β) are investigated. Numerical study is conducted with unsteady RANS simulation due to the highly unsteady flow of the tip vortex induced by the low aspect ratio swept control surface and the vortex generated by the gap between the control surface root and the wall. The high fidelity in-house CFD code FASIP with the Improved Delayed Detached Eddy Simulation (IDDES) turbulence modeling is utilized [30, 31, 32].

1.1 Co-Flow Jet

In the CFJ wing, an injection slot near leading edge (LE) and a suction slot near trailing edge (TE) on the wing suction surface are created as shown in Fig. 1. A small amount of mass flow is drawn into the wing near the TE, pressurized and energized by a micro-compressor pumping system inside the airfoil, and injected near the LE in tangent to the main flow. The whole process does not add any mass flow to the system and hence is a ZNMF flow control.

Downloaded by Gecheng Zha on June 22, 2019 | http://arc.aiaa.org | DOI: 10.2514/6.2019-3168

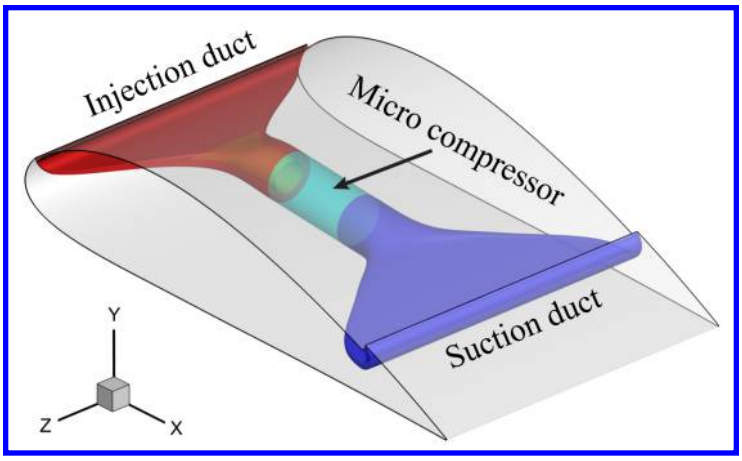

Figure 1: Schematics of CFJ wing

Downloaded by Gecheng Zha on June 22, 2019 | http://arc.aiaa.org | DOI: 10.2514/6.2019-3168

A symmetric CFJ airfoil is used for the control surface as shown in Fig.2. The injection slot and the suction slot are distributed on both sides of control surface CFJ airfoil. When one side CFJ is working to generate side force, the other side CFJ is closed. The 3D CFJ control surface is created by extruding and tapering the 2D CFJ airfoil in spanwise direction.

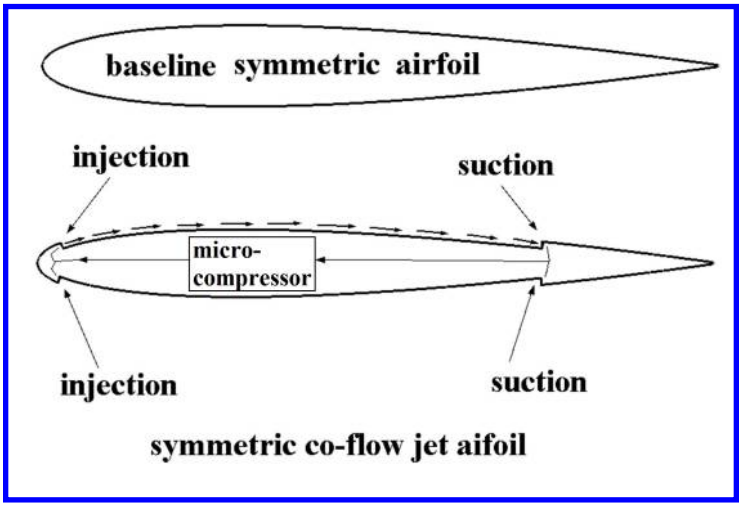

Figure 2: Schematics of CFJ control surface airfoil

2 CFJ Parameters

This section lists the important parameters used to evaluate aerodynamic performance of a CFJ airfoil.

2.1 Jet Momentum Coefficient

The jet momentum coefficient C_μ is a parameter used to quantify the jet intensity. It is defined as:

$$C_\mu = \frac{\dot{m} V_j}{\frac{1}{2}\rho_\infty {V_\infty}^2 S} \tag{1}$$

where $\dot{m}$ is the injection mass flow, V_j is the mass-averaged injection velocity, ρ_∞ and V_∞ denote the free stream density and velocity, and S is the planform area.

2.2 Lift and Drag Calculation

For CFD simulation, the full reactionary forces produced by the momentum and pressure at the injection and suction slots are included by using control volume analysis. Zha et al.[33] give the following formulations to calculate the lift and drag due to the jet reactionary force for a CFJ airfoil. By considering the effects of injection and suction jets on the CFJ airfoil, the expressions for these reactionary forces are given as :

$$F_{x_{cfj}} = (\dot{m}_j V_{j1} + p_{j1} A_{j1}) * cos(\theta_1 - \alpha) - (\dot{m}_j V_{j2} + p_{j2} A_{j2}) * cos(\theta_2 + \alpha) \tag{2}$$

$$F_{y_{cfj}} = (\dot{m}_{j1} V_{j1} + p_{j1} A_{j1}) * sin(\theta_1 - \alpha) + (\dot{m}_{j2} V_{j2} + p_{j2} A_{j2}) * sin(\theta_2 + \alpha) \tag{3}$$

where the subscripts 1 and 2 stand for the injection and suction respectively, and θ_1 and θ_2 are the angles between the injection and suction slot's surface and a line normal to the airfoil chord. α is the angle of attack.

The total lift and drag on the airfoil can then be expressed as:

$$D = R'_x - F_{x_{cfj}} \tag{4}$$

$$L = R'_y - F_{y_{cfj}} \tag{5}$$

where R'_x and R'_y are the surface integral of pressure and shear stress in x (drag) and y (lift) direction excluding the internal ducts of injection and suction. For CFJ wing simulations, the total lift and drag are calculated by integrating Eqs.(4) and (5) in the spanwise direction.

2.3 Power Coefficient

CFJ is implemented by mounting a pumping system inside the wing that withdraws air from the suction slot and blows it into the injection slot. The power consumption is determined by the jet mass flow and total enthalpy change as the following:

$$P = \dot{m}(H_{t1} - H_{t2}) \tag{6}$$

Downloaded by Gecheng Zha on June 22, 2019 | http://arc.aiaa.org | DOI: 10.2514/6.2019-3168

where H_{t1} and H_{t2} are the mass-averaged total enthalpy in the injection cavity and suction cavity respectively, P is the power required by the pump and $\dot{m}$ the jet mass flow rate. Introducing P_{t1} and P_{t2} the mass-averaged total pressure in the injection and suction cavity respectively, the pump efficiency η, and the total pressure ratio of the pump $\Gamma = \frac{P_{t1}}{P_{t2}}$, the power consumption is expressed as:

$$P = \frac{\dot{m} C_p T_{t2}}{\eta} (\Gamma^{\frac{\gamma-1}{\gamma}} - 1) \tag{7}$$

where γ is the specific heat ratio equal to 1.4 for air. The power coefficient is expressed as:

$$P_c = \frac{P}{\frac{1}{2}\rho_\infty V_\infty^3 S} \tag{8}$$

2.4 Corrected Aerodynamic Efficiency

The conventional wing aerodynamic efficiency is defined as:

$$\frac{L}{D} \tag{9}$$

For the CFJ wing, the ratio above still represents the pure aerodynamic relationship between lift and drag. However, since CFJ active flow control consumes energy, the ratio above is modified to take into account the energy consumption of the pump. The formulation of the corrected aerodynamic efficiency for CFJ wings is:

$$(\frac{L}{D})_c = \frac{C_L}{C_D + P_c} \tag{10}$$

where P_c is the power coefficient, L and D are the lift and drag generated by the CFJ wing. The formulation above converts the power consumed by the CFJ into a force $\frac{P}{V_\infty}$ which is added to the aerodynamic drag D. If the pumping power is set to 0, this formulation returns to the aerodynamic efficiency of a conventional wing.

3 The Numerical Algorithm

The in-house high accuracy CFD code Flow-Acoustics-Structure Interaction Package (FASIP) is used to conduct the numerical simulation. The 3D Improved Delayed Detached Eddy Simulation (IDDES) [30, 31, 32] turbulence model is used. A 5th order WENO scheme for the inviscid flux [34, 35, 36, 37, 38, 39] and a 2nd order central differencing for the viscous terms [34, 38] are employed to discretize the Navier-Stokes equations. The low diffusion Roe scheme used as the approximate Riemann solver is utilized with the WENO scheme to evaluate the inviscid fluxes. Implicit time marching method using Gauss-Seidel line relaxation is used to achieve a fast convergence rate [39]. Parallel computing is implemented to save wall clock simulation time [40]. The FASIP code is intensively validated for CFJ airfoil simulations [2, 5, 19, 20, 21, 22, 23, 24, 25, 26, 27, 28]. Since the experimental results reported are time averaged steady state results, the numerical results are also presented as the time averaged results of the last 200 time steps when the flow and all the aerodynamic forces become statistically stable.

Downloaded by Gecheng Zha on June 22, 2019 | http://arc.aiaa.org | DOI: 10.2514/6.2019-3168

4 Baseline Control Surface Validation

The baseline 3D vertical tail with no flow control tested and simulated in [9, 10, 11, 12, 41] is used as the baseline for this study for comparison. The baseline vertical tail is tapered, swept at 42 ° and stacked using NACA0012 airfoil. It has a 35% chord of flap length, a span of 1.067m and a mean aerodynamic chord (MAC) of 0.538m and a flap deflection angle of 30°. In the testing control surface model, there is a very small gap between the front main control surface and the flap when the flap is deflected. This small gap is considered as insignificant to affect the 3D control surface aerodynamic performance and is thus not simulated in this study.

The computational conditions use the same freestream conditions given by Seele et al in the experiment [12], which has the free stream conditions of Re_∞=1.36×10^6, U_∞=40 m/s (about Mach 0.12), and sideslip angle β=0° and 7.5°.

The mesh topology is shown in Fig. 3. The computational domain is meshed using O-type grid with the mesh size of 6.14 million points (480 × 80 × 160). Mesh refinement studies were also conducted by doubling the number of grid points in i, j, k direction respectively as 960 × 80 × 160, 480 × 160 × 160 and 480 × 80 × 320. The zero gradient condition is applied at farfield in the span direction away from the tip. Radial farfield has 30 times chords length, where the total pressure, total temperature and flow angle are specified at the farfield inlet and the static pressure is specified at the outlet to match the freestream Mach number. The boundary conditions set-up at wing root domain are illustrated in Fig. 4. A no-slip wall condition is imposed on the domain around the wing root to simulate the wind tunnel testing condition, whereas the outer root domain uses the symmetry boundary condition. This set-up is similar to the boundary condition used in [41]. For all other solid wall surfaces, the no slip wall boundary condition is used.

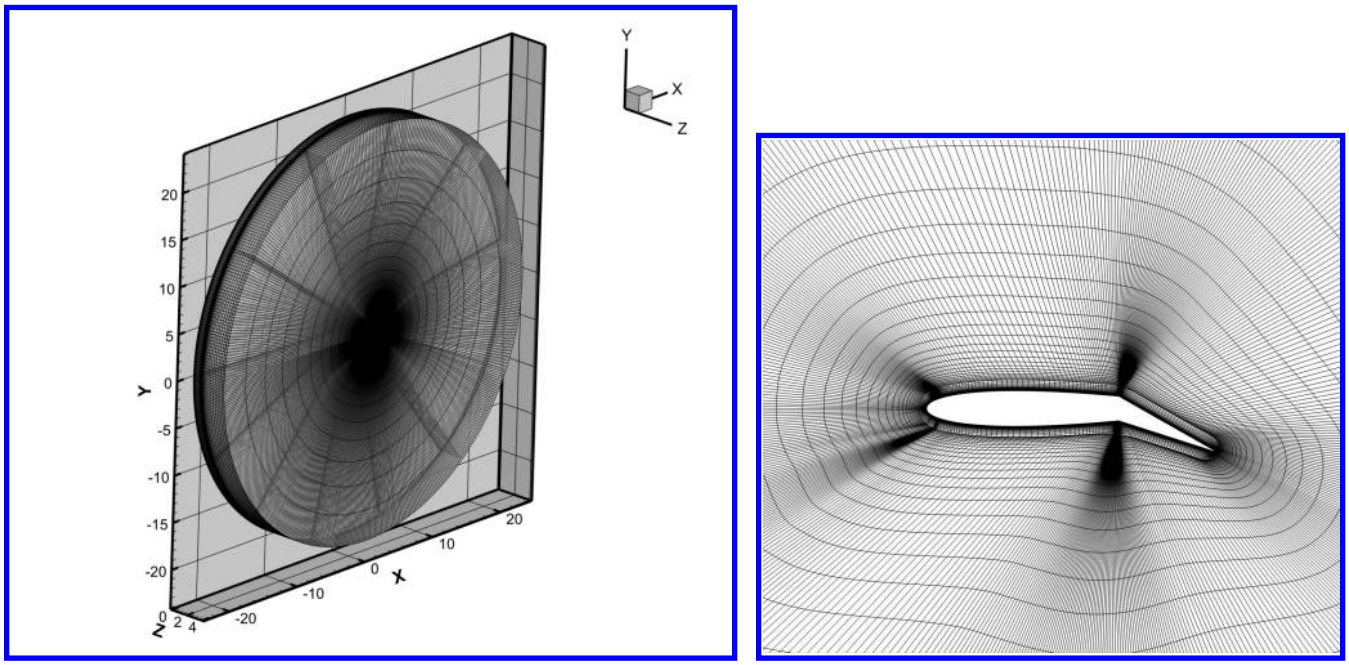

(a) Computational mesh (b) Mesh at cross section

Figure 3: Mesh topology of control surface

Downloaded by Gecheng Zha on June 22, 2019 | http://arc.aiaa.org | DOI: 10.2514/6.2019-3168

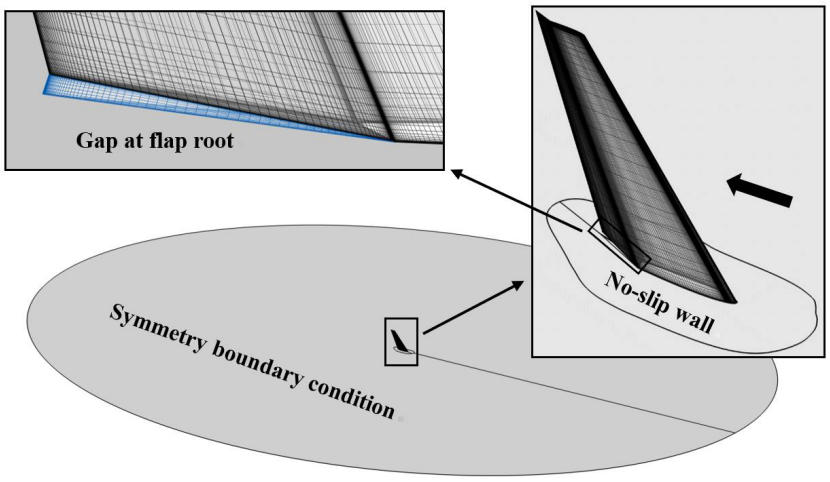

Figure 4: Boundary conditions and mesh details at wing root

Table 1 shows the C_L and C_D comparison between the experiment and the CFD simulations. A good agreement is achieved using the baseline mesh with C_L deviation of 3.8% and C_D deviation of 3.3%. Mesh refinement results show that the maximum discrepancy for the lift coefficient is 2.1% and for the drag is 2.7%, which indicates that the baseline mesh is reasonably converged and is acceptable.

Table 1: Simulations of baseline control surface

Cases	Mesh size	β (deg)	$Re{\times}10^6$	C_L	C_D
Experiment measurement	-	0	1.36	0.78	0.112
Baseline mesh	480 × 80 × 160	0	1.36	0.750	0.108
Doubled in i-direction	960 × 80 × 160	0	1.36	0.734	0.108
Doubled in j-direction	480 × 160 × 160	0	1.36	0.753	0.105
Doubled in k-direction	480 × 80 × 320	0	1.36	0.745	0.105

The computed results are further validated by examining the wing surface pressure coefficient distribution. Three spanwise locations shown in Fig. 5 are selected for comparison, inboard (40% span of at LE), middle (70% span of at LE) and outboard (89% span of at LE). Fig. 6 shows that the experimental and predicted pressure coefficient agree very well for all the three spans. Excellent agreement between the predicted and experiment pressure are obtained up to 65% chord from the leading edge since there is no flap and no flow separation. The deviation is more at the flap, which has a flow separation at a deflection angle of 30°. For the inboard and outboard location, the root vortex and tip vortex also affect the numerical results.

Downloaded by Gecheng Zha on June 22, 2019 | http://arc.aiaa.org | DOI: 10.2514/6.2019-3168

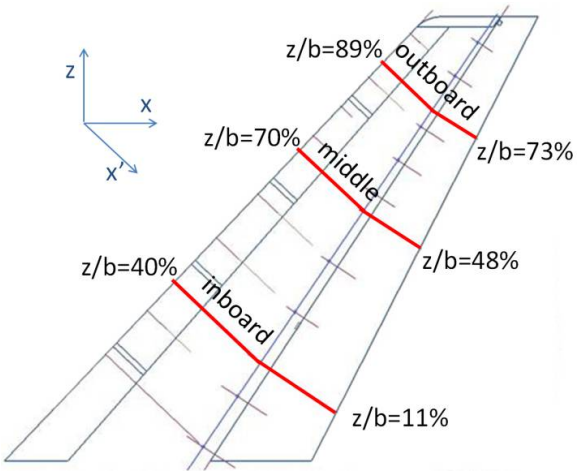

Figure 5: Illustration of spanwise pressure tap rows (picture adopted from [41])

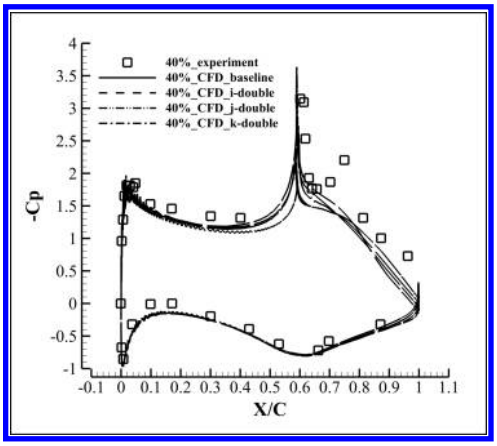

(a) $-C_p$ at inboard span

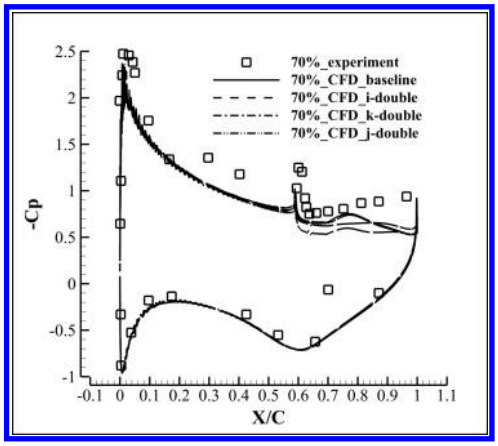

(b) $-C_p$ at middle span

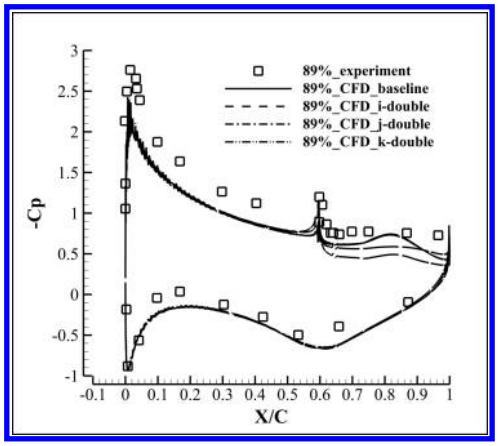

(c) $-C_p$ at outboard span

Figure 6: Negative pressure coefficient ($-C_p$) distributions of baseline control surface

Fig. 7 (a), (b), and (c) show the Mach contours of the baseline control surface at the three span locations corresponding to Fig. 5 at 40% span, 70% span and 89% span. They clear display the flow separation at the 30° deflected flap. Fig. 7 (d) show the overall streamlines colored by Mach number. The massive flow separation on the flap forms a vortex tube rolling upward and connecting to the tip vortex.

Downloaded by Gecheng Zha on June 22, 2019 | http://arc.aiaa.org | DOI: 10.2514/6.2019-3168

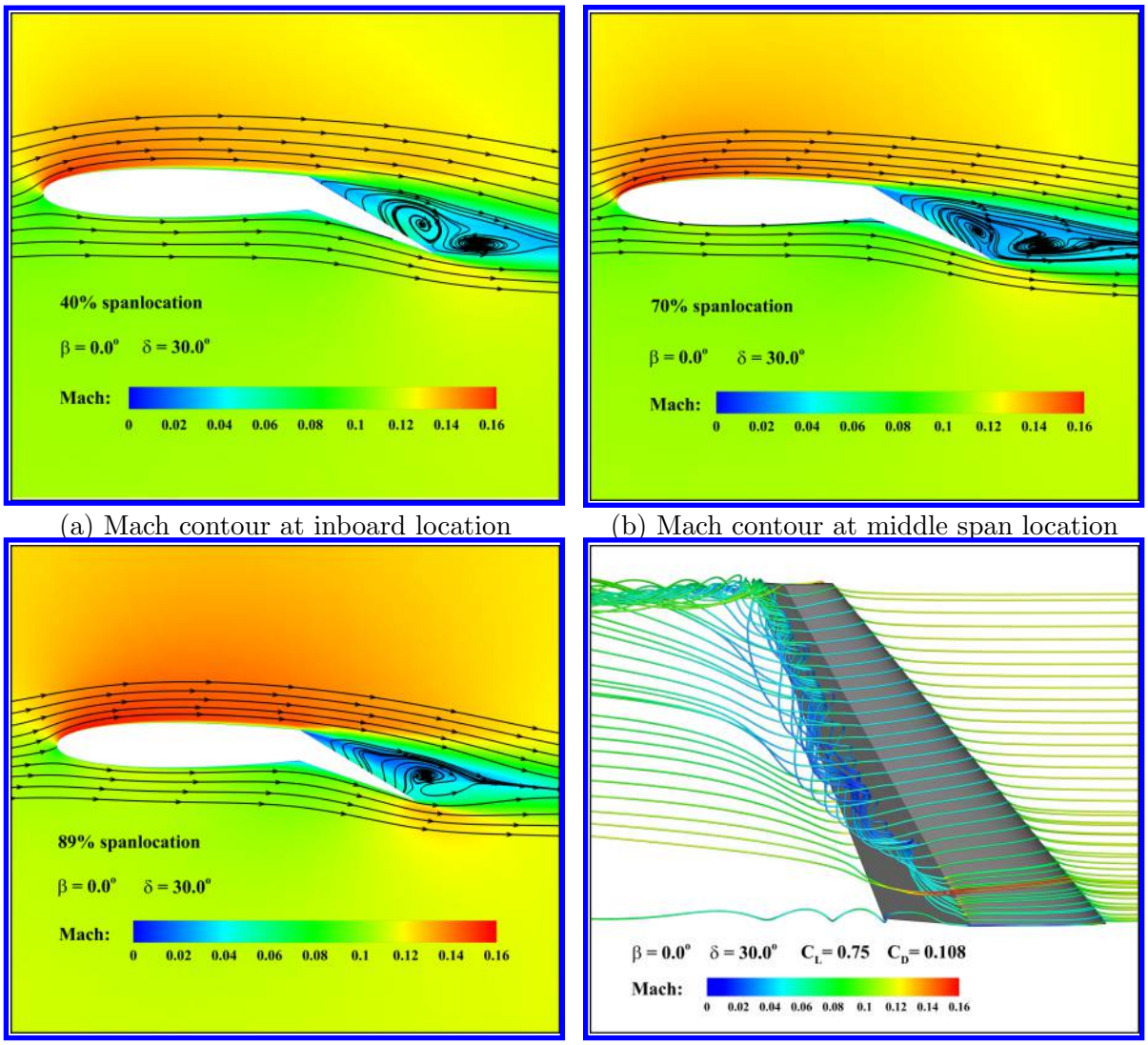

(a) Mach contour at inboard location (b) Mach contour at middle span location

(c) Mach contour at outboard location (d) 3D streamlines of baseline control surface

Figure 7: Flow field details of baseline control surface

Downloaded by Gecheng Zha on June 22, 2019 | http://arc.aiaa.org | DOI: 10.2514/6.2019-3168

5 3D CFJ Control Surface

The 3D CFJ control surface shown in Fig. 8 is created based on the baseline wing by adding injection slots (red) near the leading edge and suction slots (blue) right upstream of flap location. The basic CFJ control airfoil is the same as the one shown in the lower part of Fig. 2. Since only one side of CFJ is simulated, the injection and suction slots are created only on one side of the control surface. The CFJ slots on the other side are treated as steps to represent the closed slot conditions as the green part shown in Fig. 8. In the present study, the injection slot is located at 4% chord and the suction slot locates at 63% chord from the LE.

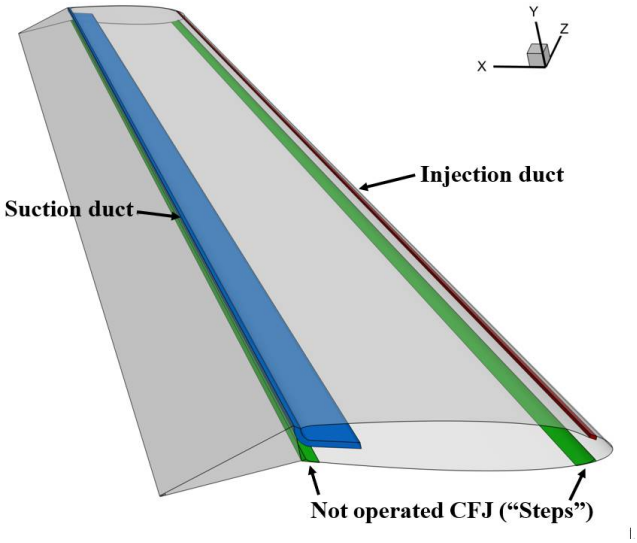

Figure 8: 3D CFJ control surface

Fig. 9 the is the cross section of 3D CFJ control surface. In our typical simulations, the simulated injection mass will flow through an internal channel as illustrated in yellow color in Fig. 9 . However, in this study, the injection duct is shortened at near the injection slot as shown in red color in Fig. 9. The reason is that a short duct near the injection slot is easier to control the jet to be aligned with the main flow when the wing has a large sweep angle. Otherwise, the flow will have a deflection after hitting the swept duct turning wall as illustrated by the streamlines in Fig. 10 . It is more time consuming to adjust the flow incidence hitting the turning duct wall so that the deflection can be aligned with the main flow. The short duct adopted is a numerical treatment to focus on the effect of the CFJ and leave the details of the jet deflection alignment as future work.

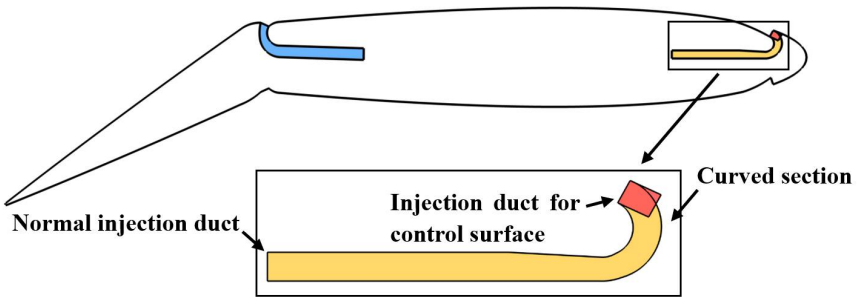

Figure 9: Cross section of 3D control surface

Downloaded by Gecheng Zha on June 22, 2019 | http://arc.aiaa.org | DOI: 10.2514/6.2019-3168

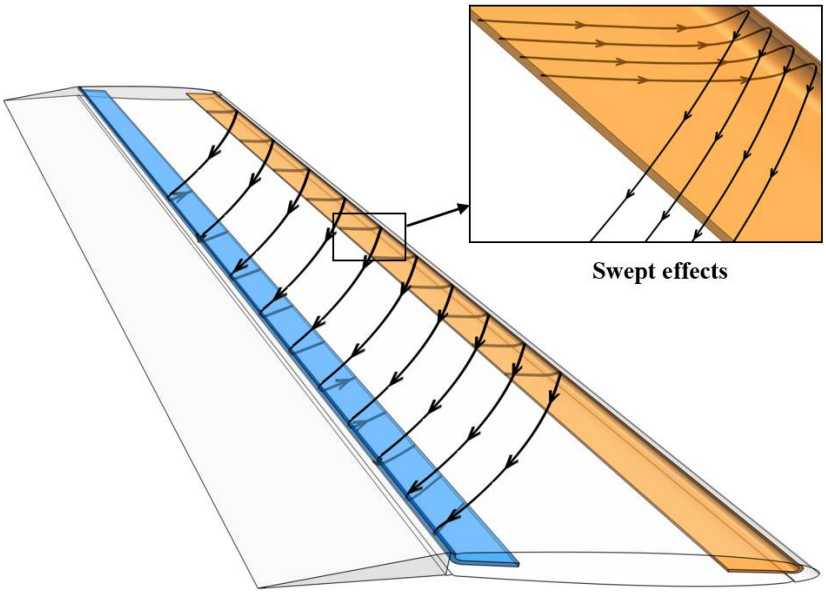

Figure 10: Illustration of swept effects

5.1 Jet Momentum Coefficient (C_μ) Variation

Four jet momentum coefficients of C_μ=0.025, 0.05, 0.1, and 0.26 are studied with the sideslip angle (β) fixed at 0° and the flap deflection angle (δ) fixed at 30°. Table 2 compares the aerodynamic parameters between the non-controlled baseline and CFJ control surface. Substantial C_L enhancement is achieved for all the CFJ control surfaces. The increase of C_μ augments the C_L, the power coefficient P_c, and the aerodynamic ratio of lift to drag (C_L/C_D). It significantly decreases the drag coefficient while increasing the lift coefficient due to the CFJ super-suction effect. The overall corrected aerodynamic efficiency $(C_L/C_D)_c$ is decreased due to the more rapid increase of the CFJ power coefficient when the C_μ and lift coefficient are increased. As the C_μ is increased from 0.025 to 0.1, the drag coefficient is about the same. When the C_μ is increased to 0.26, the drag coefficient is sharply decreased due to the super-suction effect at the wing leading edge. It is noted that at a low C_μ of 0.025, the C_L is increased by 28% compared to the baseline, but $(C_L/C_D)_c$ is also slightly increased.

At the same time, increasing the lift coefficient is the main objective, CFJ control surface with C_μ of 0.26 achieves a C_L of 1.494, about twice of the baseline control surface lift coefficient. This means that the CFJ control surface size can be half of the baseline one. For the C_μ of 0.26 case, the corrected aerodynamic efficiency is also substantially decreased by 65%. In other words, it comes with a price of costing more energy to achieve such a high lift. Since the control surface may be used for a very short transient time, the total energy consumed by the control surface may hence be negligible compared to the size, drag and weight reduction benefit brought to the aircraft for the whole mission.

Downloaded by Gecheng Zha on June 22, 2019 | http://arc.aiaa.org | DOI: 10.2514/6.2019-3168

Table 2: Aerodynamic performance of control surface with different C_μ

Cases	β (deg)	C_L	C_D	P_c	C_L/C_D	$(C_L/C_D)_c$
Baseline	0	0.750	0.108	-	6.93	6.93
C_μ=0.025	0	0.961	0.109	0.026	8.84	7.09
C_μ=0.05	0	1.13	0.116	0.054	9.72	6.64
C_μ=0.1	0	1.30	0.1095	0.198	11.9	4.23
C_μ=0.2	0	1.45	0.077	0.507	18.8	2.48
C_μ=0.26	0	1.49	0.05	0.768	28.8	1.82

Fig. 11 shows the streamlines of the baseline and CFJ control surfaces with C_μ of 0.025. It shows that the baseline control surface (left) has trailing edge spanwise vortex formed starting from the root vortex connected to the tip vortex. With a small C_μ of 0.025, the trailing edge spanwise vortex structure is removed due to no flow separation even though the streamlines are still swept toward the tip. The root and tip vortices become weaker. This benefits the control surface with the lift coefficient increased by 28% without increasing the total drag coefficient as indicated in Table 2. The low CFJ power coefficient due to the small C_μ increases the system overall corrected aerodynamic efficiency.

Downloaded by Gecheng Zha on June 22, 2019 | http://arc.aiaa.org | DOI: 10.2514/6.2019-3168

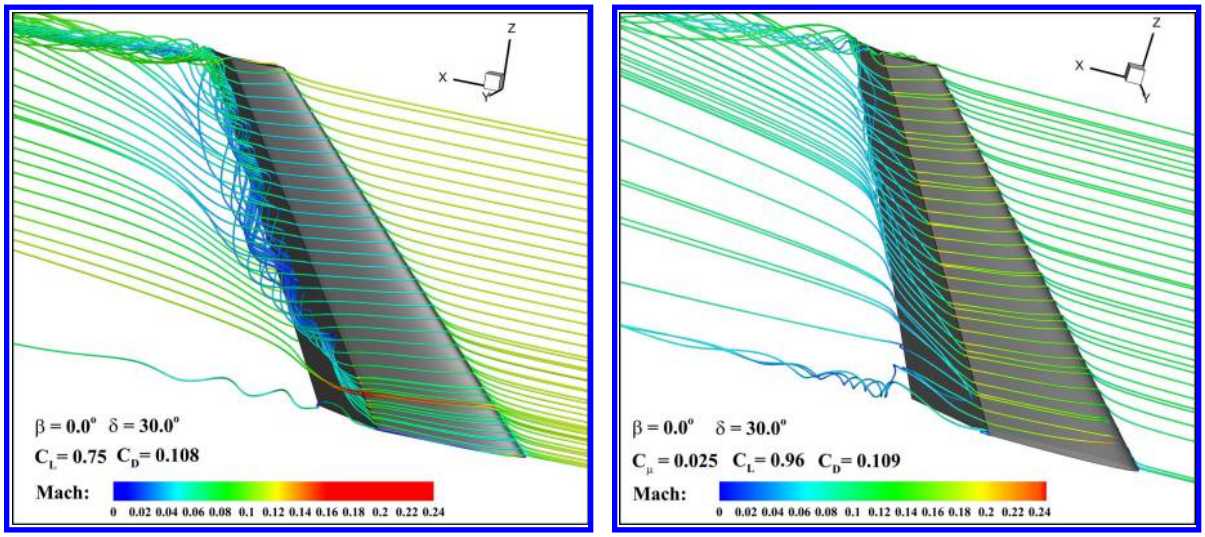

(a) Baseline (b) CFJ case with C_μ=0.025

Figure 11: Streamlines of baseline and CFJ control surface

With the C_μ increased to 0.26 as shown in Fig. 12 (a), not just the trailing edge spanwise vortex is removed, the streamlines are very well aligned with the freestream direction with little sweep toward to the tip. As expected, the lift coefficient is increased by 99% from 0.75 to 1.49 with the drag coefficient reduced by 54% from 0.108 to 0.05. The Mach contour in Fig. 12 (b) also shows that the injection Mach number reaches 0.74, which increases the CFJ power coefficient substantially with the $(C_L/C_D)_c$ reduced to 2.48 as shown in Table 2. The lift coefficient can be continuously increased, but the power coefficient will be also increased rapidly.

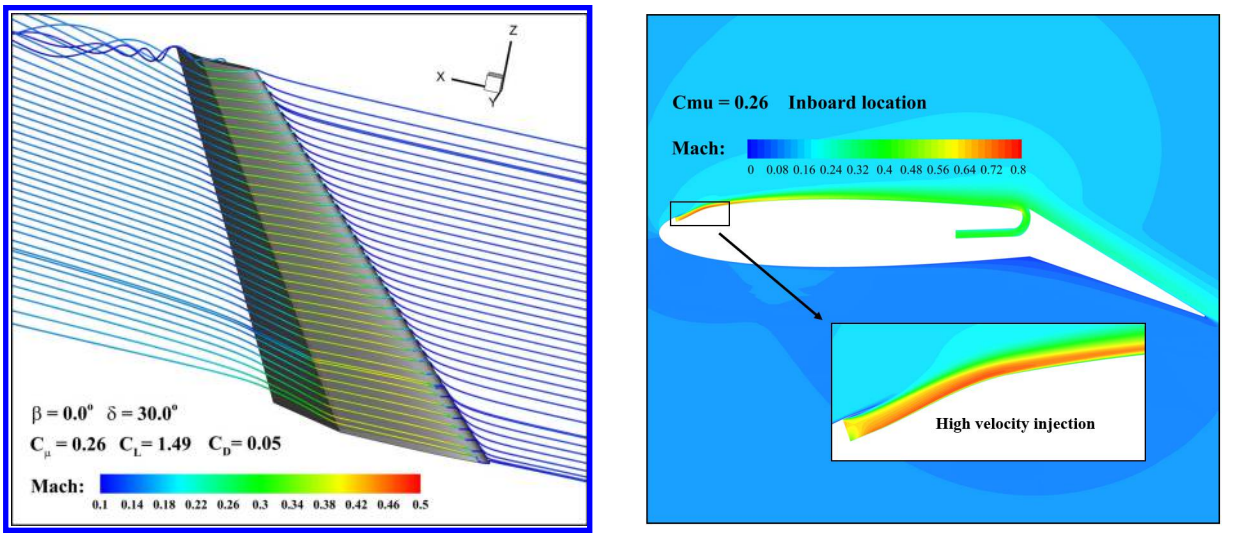

(a) CFJ case with C_μ=0.26 (b) Mach contour at inboard location of C_μ=0.26

Figure 12: Flow details of CFJ control surface with C_μ=0.26

Fig. 13 shows the C_p comparison between the baseline and CFJ control surfaces. The higher the C_μ, the larger the area enclosed by the C_p line. The suction effect largely contributing to the lift enhancement is at two locations, the leading edge due to the CFJ injection effect and the flap deflection location due to the CFJ jet suction effect. A phenomenon not observed in the regular CFJ wings without flaps is that the second pressure suction peak at the flap deflection location is higher than the leading edge suction peak. This phenomenon also exists for the baseline control surface as shown in Fig. 6 , but only at the inner span. The leading edge suction peak is dominant at the mid and outer span. For the CFJ control surface as shown in Fig. 13, the second suction peak is higher than the leading edge suction peak for all the three span locations. This phenomenon occurs for all the C_μ values and from the inner board to the outer board. This appears to be attributed to two reasons: 1) The low pressure from the jet suction slot decreases the local pressure. 2) The attached flow experiences a rapid turning due to the flap deflection, which creates a local acceleration that further reduces the pressure, as shown in Fig. 14.

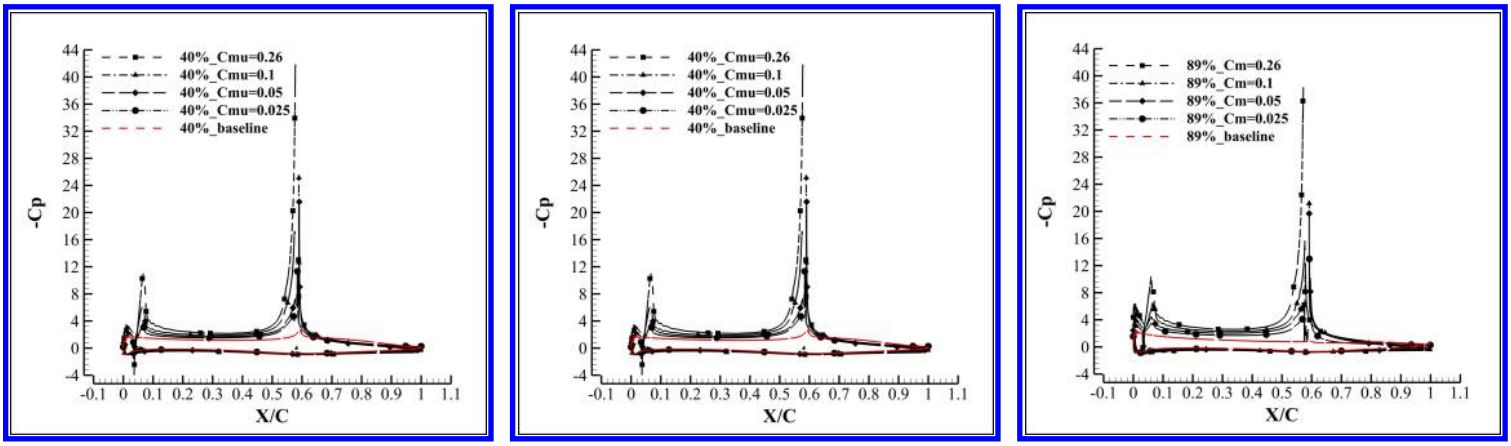

(a) Inboard span $-C_p$ comparison (b) Middle span $-C_p$ comparison (c) Outboard span $-C_p$ comparison

Figure 13: Negative pressure coefficient ($-C_p$) distributions of CFJ control surfaces

Downloaded by Gecheng Zha on June 22, 2019 | http://arc.aiaa.org | DOI: 10.2514/6.2019-3168

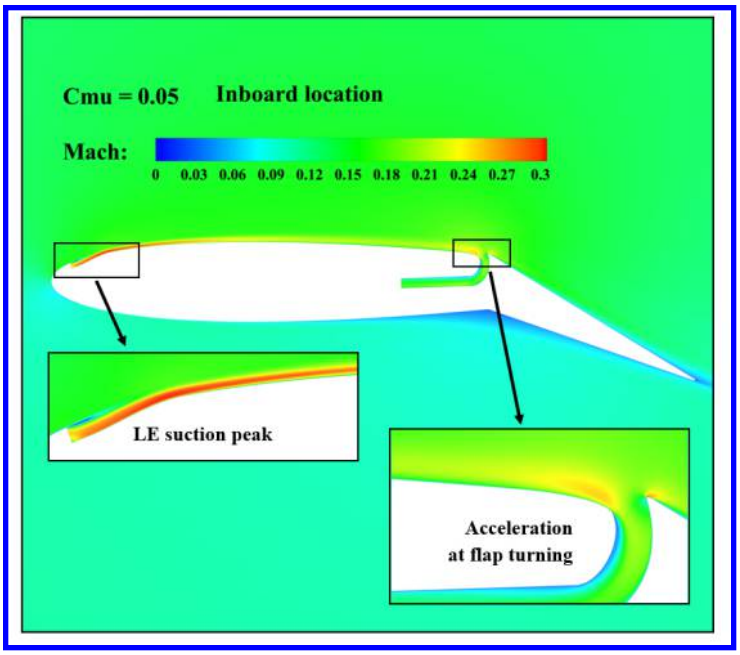

Figure 14: Mach contour at inboard cross section with C_μ=0.05

5.2 Sideslip Angle (β) Variation

The baseline and CFJ control surface with varying sideslip angles (β) are studied in this section. The flap deflection angle (δ) is fixed at 30° and the studied C_μ are 0.025, 0.05 and 0.26. Fig. 15 plots lift coefficient (C_L) and aerodynamic efficiency (C_L/C_D) versus sideslip angle. As it shows, the baseline control surface stalls at β=12.5°, whereas the CFJ control surfaces achieve the stall angle of 17.5° at C_μ=0.05 and 27.5 ° at C_μ=0.26. Considering the flap angle of 30°, the angle of attack (AoA) of the CFJ control surface is 57.5° at β of 27.5°. Fig. 16 presents the streamlines at such high AoA. The flow is very well attached along major portion of the CFJ rudder flap and minor flow separation is observed at tip region due to the interaction of spanwise flow and tip vortex.

Downloaded by Gecheng Zha on June 22, 2019 | http://arc.aiaa.org | DOI: 10.2514/6.2019-3168

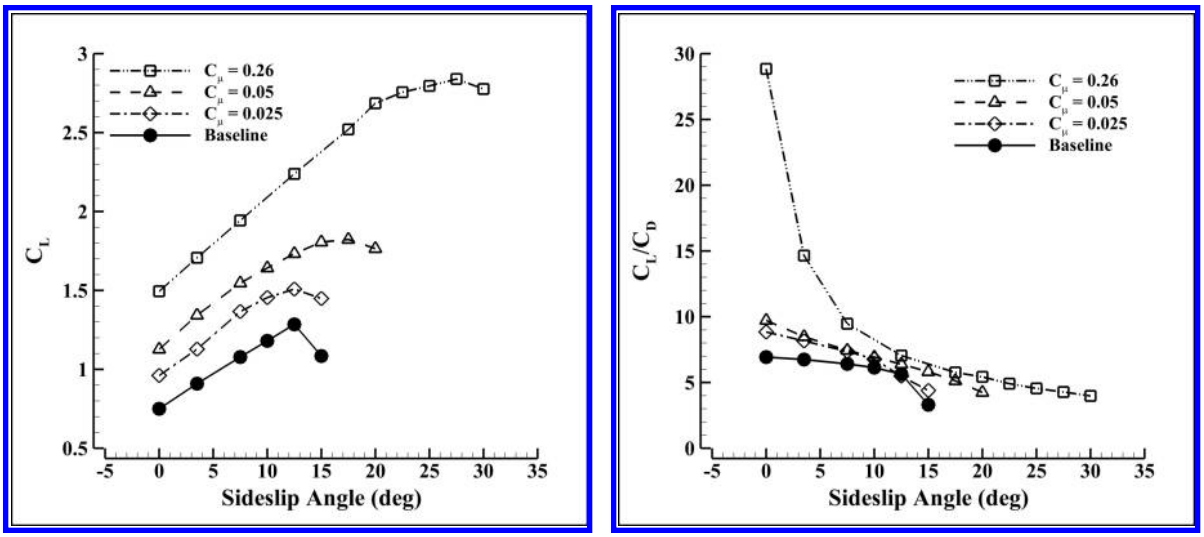

(a) Plots of C_L with different β angles (b) Plots of C_L/C_D with different β angles

Figure 15: Lift coefficient (C_L) and aerodynamic efficiency (C_L/C_D) plots

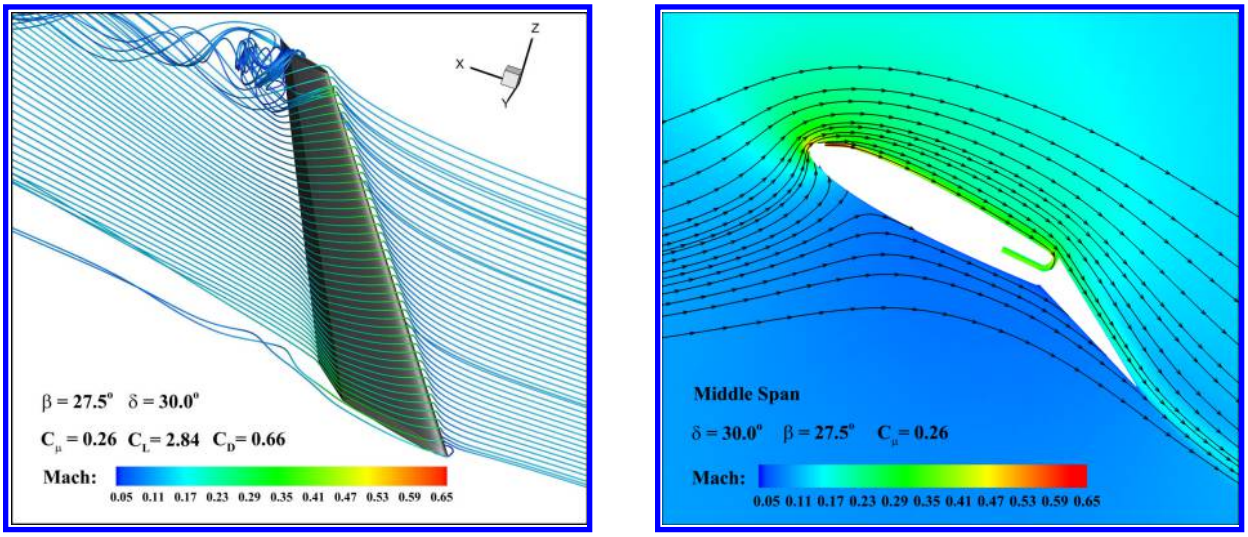

(a) Streamlines of CFJ rudder at β=27.5°, C_μ=0.26 (b) Middle span streamlines

Figure 16: Streamlines of CFJ rudder at highest β angle

Fig. 17 plots the corrected aerodynamic efficiency ($(C_L/C_D)_c$) and power coefficient (P_c) of the CFJ control surfaces with the variation of β. Fig. 17 (a) shows that at low C_μ=0.025 and 0.05, $(C_L/C_D)_c$ decreases as β angle increases. However at high C_μ=0.26, $(C_L/C_D)_c$ first increases to a peak value at β=12.5° and then decreases until stall. This pattern can be explained by the characteristic of P_c plots shown in Fig. 17 (b). In high C_μ, $(C_L/C_D)_c$ is dominated by P_c term. The higher the P_c, the lower the $(C_L/C_D)_c$. As β angle increases, leading edge suction peak is gradually enhanced, which decreases local static pressure and results in lower power consumption for CFJ injection. Once β angle passes 12.5°, the boundary layer is significantly deteriorated by the severe adverse pressure gradient and suffers a very large loss. The power required to pump the CFJ is thus increased substantially at higher β angle.

Downloaded by Gecheng Zha on June 22, 2019 | http://arc.aiaa.org | DOI: 10.2514/6.2019-3168

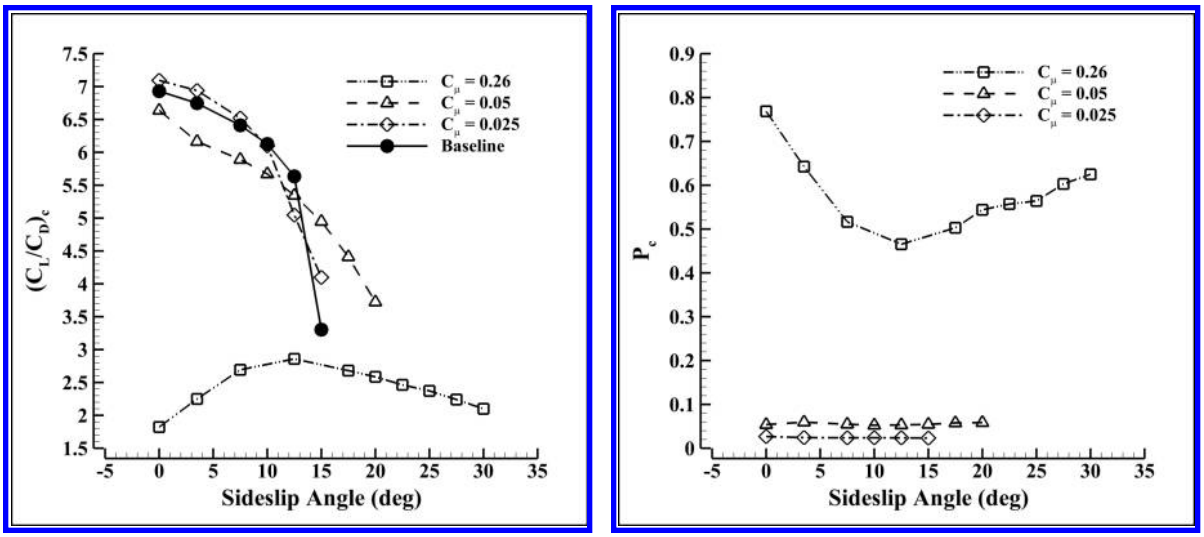

(a) Plots of $(C_L/C_D)_c$ at different β angles (b) Plots of P_c at different β angles

Figure 17: Corrected aerodynamic efficiency ($(C_L/C_D)_c$) and Power coefficient (P_c) plots

5.3 Deflection Angle (δ) Variation

The CFJ control surfaces with δ=30°, 40° and 50° are studied in this section. The sideslip angle (β) is fixed at 0° and C_μ ranges from 0.025 to 0.26. Table 3-5 present the aerodynamic performance of the control surfaces with all the studied deflection angles. Fig.18 (a), (b), and (c) plot the C_L, C_L/C_D, and $(C_L/C_D)_c$ of the three deflection angles at various C_μ. Given the same C_μ, the higher the deflection angle, the larger the increment of C_L. But this pattern is not held at low C_μ ranging from 0.025 to 0.1, because at high δ angle of 40° and 50°, a small C_μ is no longer enough to attach the flow. As shown in Fig.19 (a) and (b), the flow is separated at C_μ of 0.025 and δ at 40deg and 50deg. At high C_μ of 0.26, the flow is fully attached on the flap as shown in Fig.19 (c) and (d) and a very high C_L of 1.88 and 2.12 is achieved at 0° sideslip angle with δ of 40° and 50° respectively.

Table 3: Aerodynamic performance of control surfaces at δ=30° and different C_μ

Cases	β (deg)	C_L	C_D	P_c	C_L/C_D	$(C_L/C_D)_c$
Baseline	0	0.750	0.108	-	6.93	6.93
C_μ=0.025	0	0.961	0.109	0.026	8.84	7.09
C_μ=0.05	0	1.13	0.116	0.054	9.72	6.64
C_μ=0.1	0	1.30	0.1095	0.198	11.9	4.23
C_μ=0.2	0	1.45	0.077	0.507	18.8	2.48
C_μ=0.26	0	1.49	0.05	0.768	28.8	1.82

Downloaded by Gecheng Zha on June 22, 2019 | http://arc.aiaa.org | DOI: 10.2514/6.2019-3168

Table 4: Aerodynamic performance of control surfaces at δ=40° and different C_μ

Cases	β (deg)	C_L	C_D	P_c	C_L/C_D	$(C_L/C_D)_c$
Baseline	0	0.829	0.159	-	5.22	5.22
C_μ=0.025	0	0.946	0.134	0.025	7.07	5.96
C_μ=0.05	0	1.29	0.168	0.068	7.65	5.44
C_μ=0.1	0	1.56	0.194	0.171	8.07	4.29
C_μ=0.2	0	1.80	0.165	0.513	9.84	2.59
C_μ=0.26	0	1.88	0.161	0.759	11.4	2.04

Table 5: Aerodynamic performance of control surfaces at δ=50° and different C_μ

Cases	β (deg)	C_L	C_D	P_c	C_L/C_D	$(C_L/C_D)_c$
Baseline	0	0.843	0.172	-	4.90	4.90
C_μ=0.025	0	0.964	0.188	0.025	5.14	4.52
C_μ=0.05	0	1.082	0.200	0.062	5.55	4.21
C_μ=0.1	0	1.35	0.221	0.165	6.12	3.50
C_μ=0.2	0	2.00	0.304	0.528	6.59	2.41
C_μ=0.26	0	2.12	0.294	0.761	7.19	2.01

Downloaded by Gecheng Zha on June 22, 2019 | http://arc.aiaa.org | DOI: 10.2514/6.2019-3168

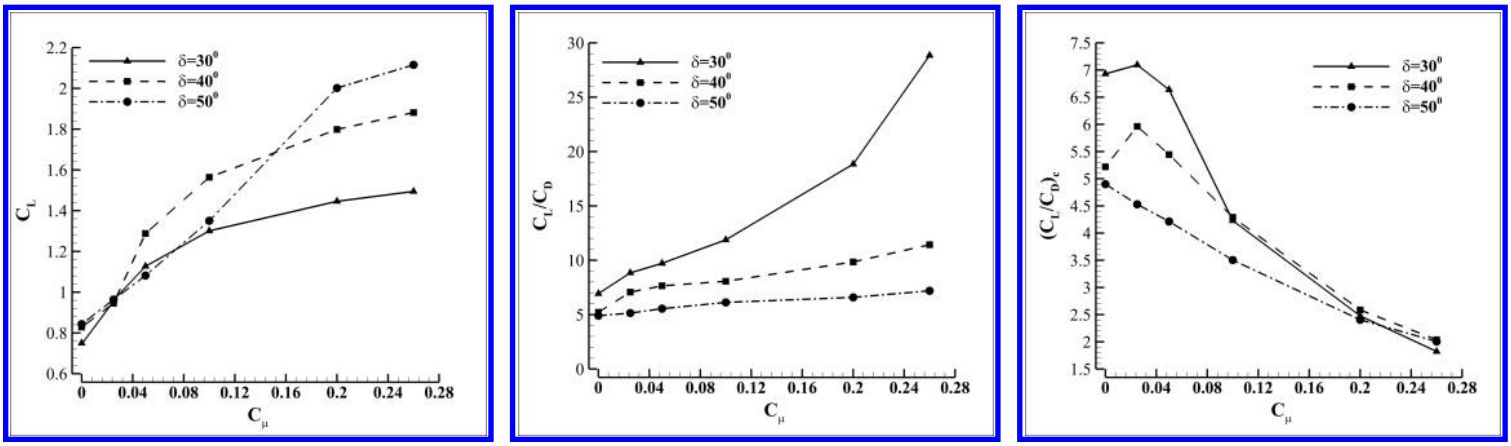

(a) C_L versus C_μ (b) C_L/C_D versus C_μ (c) $(C_L/C_D)_c$ versus C_μ

Figure 18: Aerodynamic performance of baseline and CFJ control surfaces at δ=30°, 40°, and 50°

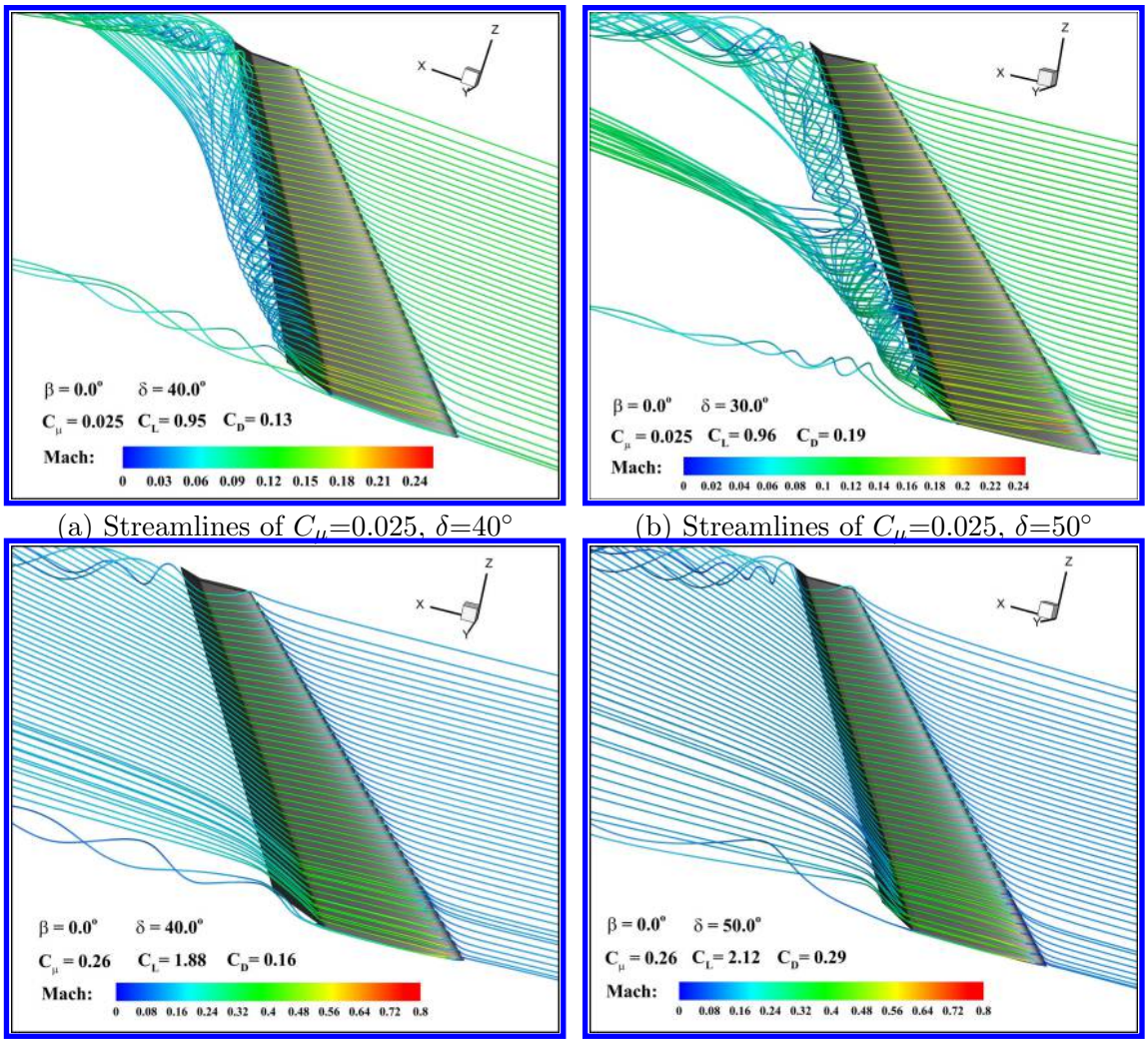

(a) Streamlines of C_μ=0.025, δ=40°

(b) Streamlines of C_μ=0.025, δ=50°

(c) Streamlines of C_μ=0.26, δ=40°

(d) Streamlines of C_μ=0.26, δ=50°

Figure 19: Streamlines of baseline and CFJ control surfaces

Downloaded by Gecheng Zha on June 22, 2019 | http://arc.aiaa.org | DOI: 10.2514/6.2019-3168

6 Conclusions

This paper numerically demonstrates that the 3D Co-flow Jet (CFJ) control surfaces can achieve ultra-high control authority with zero-net-mass-flux flow control at low energy expenditure. Numerical study is conducted with unsteady RANS simulation due to the highly unsteady flow of the tip vortex induced by the low aspect ratio swept control surface and the vortex generated by the gap between the control surface root and the wall. The effects of co-flow jet moment coefficient (C_μ), sideslip angle (β) and deflection angle (δ) are investigated. The validated results achieve a good agreement with experiment for the baseline control surface with the maximum discrepancy less than 3.8%. The numerical simulation indicates that applying Co-flow Jet on control surface is very effective and energy efficient. A small C_μ of 0.025 generates a 28% C_L increment at 0 sideslip angle with a higher corrected aerodynamic efficiency ($(C_L/C_D)_c$) than the baseline case. At the C_μ of 0.26, the C_L is increased by 99.25% at 0 sideslip angle and the C_D drops by 52% due to removal of the flow separation and suppression of the tip and root vortices by the Co-flow Jet. A phenomenon observed is that the second pressure suction peak at the flap deflection point is higher than the leading edge suction peak. It is attributed to the attached flow

experiencing a rapid turning due to the flap deflection, which creates a local acceleration that further reduces the pressure. CFJ control surface also has a much higher stall margin than baseline control surface. With C_μ=0.26, CFJ control surface stalls at the sideslip angle of 27.5°, which is 2.2 times higher than the baseline control surface of 12.5° and a very high C_L of 2.84 is also achieved at such high sideslip angle. Furthermore, a CFJ control surface can tolerate very large flap deflection angle with the flow attached and a very high lift coefficient. At C_μ=0.26 and zero sideslip angle, very high C_L of 1.88 and 2.12 are achieved at δ=40° and 50°, which are 2.3 and 2.5 times of the baseline cases respectively.

7 Acknowledgment

The authors would like to acknowledge the computing resource provided by the Center of Computational Sciences at the University of Miami. The authors would also like to express their gratitude to Dr. Veer Vatsa of NASA Langley research center and Dr. Damiano Casalino of TU Delft for the valuable discussion regarding the validation of baseline control surface simulation.

Downloaded by Gecheng Zha on June 22, 2019 | http://arc.aiaa.org | DOI: 10.2514/6.2019-3168

References

[1] S. Anders, W. Sellers III, and A. Washburn, "Active flow control activities at nasa langley," in *2nd AIAA Flow Control Conference*, AIAA 2004-2623.

[2] G.-C. Zha, B. F Carroll, C. D. Paxton, C. A. Conley, and A. Wells, "High-performance airfoil using coflow jet flow control," *AIAA journal*, vol. 45, no. 8, pp. 2087–2090, 2007.

[3] W. Bower and V. Kibens, "An overview of active flow control applications at the boeing company," in *2nd AIAA Flow Control Conference*, AIAA 2004-2624.

[4] O. Kandil, E. Gercek, X. Zheng, and X. Luo, "Development of computational sensing and active flow control of airfoils during dynamic stall," in *42nd AIAA Aerospace Sciences Meeting and Exhibit*, AIAA 2004-0043.

[5] A. Lefebvre, B. Dano, W. Bartow, M. Fronzo, and G. Zha, "Performance and energy expenditure of coflow jet airfoil with variation of mach number," *Journal of Aircraft*, vol. 53, no. 6, pp. 1757–1767, 2016.

[6] T. Van Buren and M. Amitay, "Comparison between finite-span steady and synthetic jets issued into a quiescent fluid," *Experimental Thermal and Fluid Science*, vol. 75, pp. 16–24, 2016.

[7] L. Pack, N. Schaeffler, C. Yao, and A. Seifert, "Active control of flow separation from the slat shoulder of a supercritical airfoil," in *1st Flow Control Conference*, AIAA 2002-3156.

[8] N. W. Rathay, M. J. Boucher, M. Amitay, and E. Whalen, "Performance enhancement of a vertical tail using synthetic jet actuators," *AIAA Journal*, vol. 52, no. 4, pp. 810–820, 2014.

[9] J. C. Lin, M. Y. Andino, M. G. Alexander, E. A. Whalen, M. A. Spoor, J. T. Tran, and I. J. Wygnanski, "An overview of active flow control enhanced vertical tail technology development," in *54th AIAA Aerospace Sciences Meeting*, AIAA 2016-0056.

[10] M. Y. Andino, J. C. Lin, A. E. Washburn, E. A. Whalen, E. C. Graff, and I. J. Wygnanski, "Flow separation control on a full-scale vertical tail model using sweeping jet actuators," in *53rd AIAA Aerospace Sciences Meeting*, AIAA 2015-0785.

[11] R. Seele, E. Graff, M. Gharib, L. Taubert, J. Lin, and I. Wygnanski, "Improving rudder effectiveness with sweeping jet actuators," in *6th AIAA Flow Control Conference*, AIAA 2012-3244.

[12] R. Seele, E. Graff, J. Lin, and I. Wygnanski, "Performance enhancement of a vertical tail model with sweeping jet actuators," in *51st AIAA Aerospace Sciences Meeting including the New Horizons Forum and Aerospace Exposition*, AIAA 2013-0411.

[13] N. Rathay, M. Boucher, M. Amitay, and E. Whalen, "Parametric study of synthetic-jet-based control for performance enhancement of a vertical tail," *AIAA Journal*, vol. 52, no. 11, pp. 2440–2454, 2014.

[14] E. Graff, R. Seele, J. C. Lin, and I. Wygnanski, "Sweeping jet actuators-a new design tool for high lift generation," in *NASA Technical Report Server*, 2013 20130013994.

[15] A. Shmilovich, Y. Yadlin, and E. Whalen, "Computational evaluation of flow control for enhanced control authority of a vertical tail," *AIAA Journal*, pp. 2211–2220, 2016.

[16] K. Kara, "Numerical simulation of a sweeping jet actuator," in *34th AIAA Applied Aerodynamics Conference*, AIAA 2016-3261.

[17] K. Kara, "Numerical study of internal flow structures in a sweeping jet actuator," in *33rd AIAA Applied Aerodynamics Conference*, AIAA 2015-2424.

[18] J. Zhang, K. Xu, Y. Yang, Y. Ren, P. Patel, and G. Zha, "Aircraft control surfaces using co-flow jet active flow control airfoil," in *2018 Applied Aerodynamics Conference*, AIAA 2018-3067.

[19] G. Zha, W. Gao, and C.D. Paxton, "Jet Effects on Co-Flow Jet Airfoil Performance," *AIAA Journal*, vol. 45, pp. 1222–1231, 2007.

[20] G.-C. Zha, C. Paxton, A. Conley, A. Wells, nd B. Carroll, "Effect of Injection Slot Size on High Performance Co-Flow Jet Airfoil," *AIAA Journal of Aircraft*, vol. 43, pp. 987–995, 2006.

[21] Yang, Yunchao and Zha, Gecheng, "Super-Lift Coefficient of Active Flow Control Airfoil: What is the Limit?," *AIAA SCITECH2017, 55th AIAA Aerospace Science Meeting, Grapevine, Texas*, AIAA 2017-1693.

[22] B. Wang, B. Haddoukessouni, J. Levy, and G.-C. Zha, "Numerical investigations of injection-slot-size effect on the performance of coflow jet airfoils," *Journal of Aircraft*, vol. 45, no. 6, pp. 2084–2091, 2008.

[23] B. P. E. Dano, D. Kirk, and G.-C. Zha, "Experimental Investigation of Jet Mixing Mechanism of Co- Flow Jet Airfoil." AIAA-2010-4421, 5th AIAA Flow Control Conference, Chicago, IL, 28 Jun - 1 Jul 2010.

[24] B. Dano, G. Zha, and M. Castillo, "Experimental study of co-flow jet airfoil performance enhancement using discreet jets," in *49th AIAA Aerospace Sciences Meeting including the New Horizons Forum and Aerospace Exposition*, AIAA 2011-941.

[25] Lefebvre, A. and Zha, G.-C. , "Design of High Wing Loading Compact Electric Airplane Utilizing Co-Flow Jet Flow Control." AIAA Paper 2015-0772, AIAA SciTech2015: 53nd Aerospace Sciences Meeting, Kissimmee, FL, 5-9 Jan 2015.

[26] Lefebvre, A. and Dano, B. and Bartow, W. and Di Franzo, M. and Zha, G.-C., "Performance Enhancement and Energy Expenditure of Co-Flow Jet Airfoil with Variation of Mach Number." AIAA Paper 2013-0490, AIAA Journal of Aircraft, DOI: 10.2514/1.C033113, 2016.

[27] Liu, Z.-X. and Zha, G.-C., "Transonic Airfoil Performance Enhancement Using Co-Flow Jet Active Flow Control." AIAA Paper 2016-3066, AIAA Aviation, June 13-17 2016.

Downloaded by Gecheng Zha on June 22, 2019 | http://arc.aiaa.org | DOI: 10.2514/6.2019-3168

[28] Lefebvre, A. and Zha, G.-C., "Trade Study of 3D Co-Flow Jet Wing for Cruise Performance." AIAA Paper 2016-0570, AIAA SCITECH2016, AIAA Aerospace Science Meeting, San Diego, CA, 4-8 January 2016.

[29] K. Xu, J. Zhang, and G. Zha, "Drag minimization of co-flow jet control surfaces at cruise conditions," in *AIAA Scitech 2019 Forum*, AIAA 2019-1848.

[30] P. Spalart and S. Allmaras, "A One-equation Turbulence Model for Aerodynamic Flows." AIAA-92-0439, 1992.

[31] Y. Yang and G. Zha, "Simulation of airfoil stall flows using iddes with high order schemes," in *46th AIAA Fluid Dynamics Conference*, AIAA 2016-3185.

[32] Y. Yang and G. Zha, "Improved delayed detached eddy simulation of super-lift coefficient of subsonic co-flow jet flow control airfoil," in *2018 AIAA Aerospace Sciences Meeting*, AIAA 2018-0314.

[33] G.-C. Zha, W. Gao, and C. Paxton, "Jet Effects on Co-Flow Jet Airfoil Performance," *AIAA Journal, No. 6,*, vol. 45, pp. 1222–1231, 2007.

[34] Shen, Y.Q., and Zha, G.C., "Large Eddy Simulation Using a New Set of Sixth Order Schemes for Compressible Viscous Terms," *Journal of Computational Physics*, vol. 229, pp. 8296–8312, doi:10.1016/j.jcp.2010.07.017, 2010.

[35] G.-C. Zha, Y. Shen, and B. Wang, "An improved low diffusion E-CUSP upwind scheme ," *Journal of Computer & Fluids*, vol. 48, pp. 214–220, 2011.

[36] Y.-Q. Shen, G.-C. Zha, and B.-Y. Wang, "Improvement of Stability and Accuracy of Implicit WENO Scheme ," *AIAA Journal*, vol. 47, pp. 331–344, 2009.

[37] Shen, Y.-Q. and Zha, G.-C. and Chen, X.-Y., " High Order Conservative Differencing for Viscous Terms and the Application to Vortex-Induced Vibration Flows," *Journal of Computational Physics*, vol. 228(2), pp. 8283–8300, 2009.

[38] Shen, Y.-Q. and Zha, G.-C. , " Improvement of the WENO Scheme Smoothness Estimator," *International Journal for Numerical Methods in Fluids*, vol. DOI:10.1002/fld.2186, 2009.

[39] G.-C. Zha and E. Bilgen, "Numerical study of three-dimensional flows using unfactored upwind-relaxation sweeping algorithm," *Journal of Computational Physics*, vol. 125, no. 2, pp. 425–433, 1996.

[40] B. Wang, and G.C. Zha, "A General Sub-domain Bboundary Mapping Procedure for Structured Grid CFD Parallel Computation." AIAA Paper 2007-4432, 2007.

[41] V. N. Vatsa, D. Casalino, J. C. Lin, and J. Appelbaum, "Numerical simulation of a high-lift configuration with embedded fluidic actuators," in *32nd AIAA Applied Aerodynamics Conference*, AIAA 2014-2142.

Downloaded by Gecheng Zha on June 22, 2019 | http://arc.aiaa.org | DOI: 10.2514/6.2019-3168